POLITECNICO DI TORINO
Repository ISTITUZIONALE

Development of high-speed directly-modulated DFB and DBR lasers with surface gratings.

Original
Development of high-speed directly-modulated DFB and DBR lasers with surface gratings / Dumitrescu, M.; Telkkälä, J.; Karinen, J.; Viheriälä, J.; Laakso, A.; Afzal, S.; Reithmaier, J. P.; Kamp, M.; Melanen, P.; Uusimaa, P.; Bardella, Paolo; Vallone, MARCO ERNESTO; Montrosset, Ivo; Parillaud, O.; Gready, D.; Eisenstein, G.; Sek, G.. - ELETTRONICO. - 7953:(2011). (Intervento presentato al convegno SPIE - Novel In-Plane Semiconductor Lasers tenutosi a San Francisco (U.S.A.) nel 24 january 2011) [10.1117/12.875674].

Availability:
This version is available at: 11583/2430197 since:

Publisher:
SPIE, Alexey A. Belyanin; Peter M. Smowton, editors.

Published
DOI:10.1117/12.875674

Terms of use:

This article is made available under terms and conditions as specified in the corresponding bibliographic description in the repository

Publisher copyright
SPIE postprint/Author's Accepted Manuscript e/o postprint versione editoriale/Version of Record con

Copyright 2011 Society of PhotoOptical Instrumentation Engineers (SPIE). One print or electronic copy may be made for personal use only. Systematic reproduction and distribution, duplication of any material in this publication for a fee or for commercial purposes, and modification of the contents of the publication are prohibited.

(Article begins on next page)

12 October 2024

Please verify that (1) all pages are present, (2) all figures are acceptable, (3) all fonts and special characters are correct, and (4) all text and figures fit within the margin lines shown on this review document. Return to your MySPIE ToDo list and approve or disapprove this submission.

Development of high-speed directly-modulated DFB and DBR lasers with surface gratings

M. Dumitrescu*[a], J. Telkkälä[a], J. Karinen[a], J. Viheriälä[a], A. Laakso[a],
J.-P. Reithmaier[b], M. Kamp[c], P. Melanen[d], P. Uusimaa[d], M. Rossetti[e], P. Bardella[e],
M. Vallone[e], O. Parillaud[f], D. Gready[g], G. Eisenstein[g], G. Sek[h]

[a]Optoelectronics Research Centre, Tampere University of Technology, Tampere, Finland
[b]Institute of Nanostructure technologies and Analytics, University of Kassel, Kassel, Germany
[c]Technishe Physik, University of Würzburg, Würzburg, Germany
[d]Modulight Inc., Tampere, Finland
[e]Department of Electronics, Politechnico di Torino, Torino, Italy
[f]Alcatel-Thales III-V Lab, Palaiseau, France
[g]Electrical Engineering Department, Technion, Haifa, Israel
[h]Institute of Physics, Wroclaw University of Technology, Wroclaw, Poland

ABSTRACT

The conventional distributed feedback and distributed Bragg reflector edge-emitting lasers employ buried gratings, which require two or more epitaxial growth steps. By using lateral corrugations of the ridge-waveguide as surface gratings the epitaxial overgrowth is avoided, reducing the fabrication complexity, increasing the yield and reducing the fabrication cost. The surface gratings are applicable to different materials, including Al-containing ones and can be easily integrated in complex device structures and photonic circuits. Single-contact and multiple contact edge-emitting lasers with laterally-corrugated ridge waveguide gratings have been developed both on GaAs and InP substrates with the aim to exploit the photon-photon resonance in order to extend their direct modulation bandwidth. The paper reports on the characteristics of such surface-grating-based lasers emitting both at 1.3 and 1.55 µm and presents the photon-photon resonance extended small-signal modulation bandwidth (> 20 GHz) achieved with a 1.6 mm long single-contact device under direct modulation. Similarly structured devices, with shorter cavity lengths are expected to exceed 40 GHz small-signal modulation bandwidth under direct modulation.

Keywords: distributed feedback lasers, distributed Bragg reflector lasers, surface gratings, photon-photon resonance

1. INTRODUCTION

The paper presents the progress achieved in developing high-speed distributed feedback (DFB) and distributed Bragg reflector (DBR) lasers within the EU-FP7 STREP project "Development of low-cost technologies for the fabrication of high-performance telecommunication lasers (DeLight)". Two essential novelties have been exploited in the DeLight project: the use of surface gratings, to enable a single growth and processing sweep, and the use of photon-photon resonance, to enhance the direct modulation bandwidth beyond the limits set by the carrier-photon resonance.

The conventional buried-grating DFB and DBR edge-emitting lasers require two or more epitaxial growth steps, bringing in the difficulties associated with the overgrowth, complicating the device fabrication, affecting the device performance, yiels and reliability (especially when aluminum-containing materials are used) and, ultimately, increasing the device cost. To avoid the problematic overgrowth we have employed laterally-corrugated ridge-waveguide (LC-RWG) surface gratings, illustrated in Figure 1. Since they do not require overgrowth, the LC-RWG gratings are applicable to different materials, including Al-containing ones. Also the use of surface gratings enables easy integration of the laterally-coupled DFB and DBR lasers with other devices. Moreover, the LC-RWG surface gratings have the supplementary advantage that there is only a limited interaction between the grating interfaces and the carriers, which leads to more stable devices with better performances and increased reliability.

*Mihail.Dumitrescu@tut.fi; www.orc.tut.fi

7953 - 12 V. 2 (p.1 of 12) / Color: No / Format: A4 / Date: 2011-02-03 04:15:41 PM

SPIE USE: ____ DB Check, ____ Prod Check, Notes:

Please verify that (1) all pages are present, (2) all figures are acceptable, (3) all fonts and special characters are correct, and (4) all text and figures fit within the margin lines shown on this review document. Return to your MySPIE ToDo list and approve or disapprove this submission.

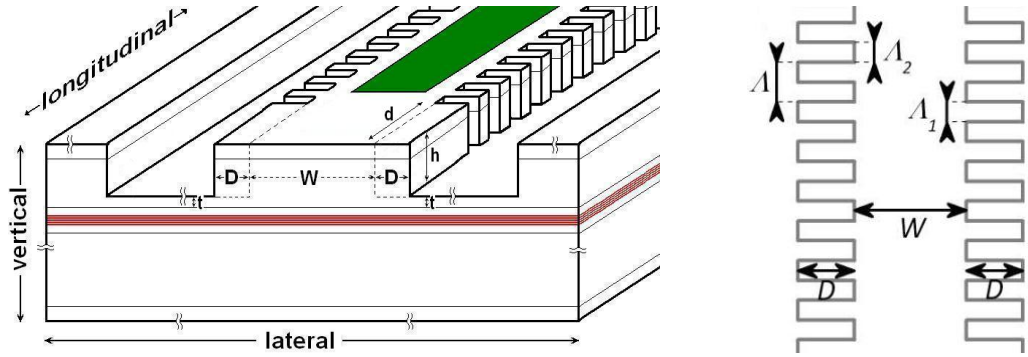

Figure 1. A 3-dimensional sketch (a) and a top view sketch (b) of the laterally-corrugated ridge-waveguide grating structure.

A LC-RWG structure sketch is given in Figure 1. The un-etched central ridge width is W, and the lateral extension of the grating corrugations is D. The etching depth is h and the un-etched p-side cladding layer thickness is t (t<0, for etching through the epitaxial waveguide region). The distances from the last/first grating period to the rear/front facet are given by d_1 and d_2 (d in the left panel of Figure 1). The lengths of the wide- and narrow-ridge grating slices are Λ_1 and Λ_2, respectively, and the grating period is $\Lambda=\Lambda_1+\Lambda_2$. Λ_2 is also called the trench width in this paper. The filling factor of the grating, γ, is Λ_1/Λ and the grating aspect ratio is h/Λ_2. The grating order is m, which is related to Λ by the Bragg condition $\Lambda=(m\cdot\lambda)/(2\cdot n_{eff})$, where n_{eff} is the effective refractive index and λ is the Bragg resonance wavelength.

Over the past several decades, substantial efforts have been undertaken to increase the direct modulation bandwidth of lasers through various methods, ranging from engineering the quantum confinement in the active medium[1-8] and utilizing injection locking techniques[8-10] to leveraging cavity quantum electrodynamics effects[11-12]. Unfortunately, despite substantial efforts, no significant breakthrough has been made when the direct modulation bandwidth has been linked to the carrier-photon resonance (CPR), largely because the CPR has inherent physical limitations. However, the direct modulation bandwidth can be substantially improved by employing the photon-photon resonance (PPR), which can be induced at the frequency separation between laser modes. Figure 2 illustrates the extended modulation bandwidth obtained by applying PPR.

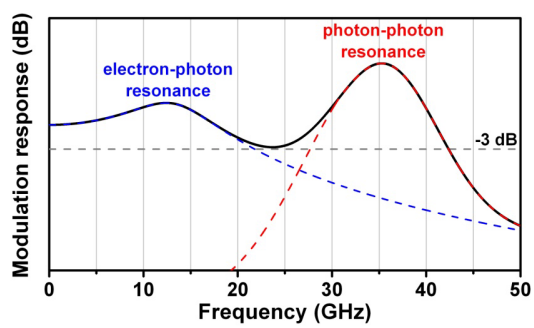

Figure 2. Extended modulation bandwidth by using the photon-photon resonance.

2. MODELING AND SIMULATION PARTICULARITIES OF THE LC-RWG GRATINGS

The coupling coefficient for gratings with rectangular-shaped longitudinal refractive index variation can be written as[13]:

$$\kappa=\frac{k_0}{2n_{eff}}\cdot\left(n_2^2-n_1^2\right)\cdot\frac{\iint_{Grating}\left|E_0(x,y)\right|^2dxdy}{\int_{-\infty}^{\infty}\int_{-\infty}^{\infty}\left|E_0(x,y)\right|^2dxdy}\cdot\frac{\sin(\pi m\gamma)}{\pi m}=\frac{k_0}{2n_{eff}}\cdot\left(n_2^2-n_1^2\right)\cdot\Gamma_g\cdot\frac{\sin(\pi m\gamma)}{\pi m} \quad (1)$$

where Γ_g is the optical confinement factor in the grating region (i.e. the fraction of the optical field intensity in the grating region) and n_1 and n_2 are the constant refractive index values in the grating regions where the optical field has a significant intensity. For buried-heterostructure gratings the coupling coefficient formula (1) is frequently simplified by

SPIE USE: ____ DB Check, ____ Prod Check, Notes:

Please verify that (1) all pages are present, (2) all figures are acceptable, (3) all fonts and special characters are correct, and (4) all text and figures fit within the margin lines shown on this review document. Return to your MySPIE ToDo list and approve or disapprove this submission.

using the approximation $n_1+n_2 \approx 2n_{eff}$, which leads to an overestimation of the coupling coefficient for LC-RWG gratings, because for these gratings $n_1+n_2 < 2n_{eff}$, as one of the alternating grating materials is a dielectric with much lower refractive index but a small influence on n_{eff}[13]. A better way for calculating the grating coupling coefficient for LC-DFB lasers is by using the definition for the effective refractive index and the better approximation $n_{eff,1}+n_{eff,2} \approx 2 \cdot n_{eff}$[13]:

$$\kappa = \frac{k_0}{2n_{eff}} \cdot (n_{eff,2}{}^2 - n_{eff,1}{}^2) \cdot \frac{\sin(\pi m \gamma)}{\pi m} \approx k_0 \cdot (n_{eff,2} - n_{eff,1}) \cdot \frac{\sin(\pi m \gamma)}{\pi m} = \frac{2 \cdot (n_{eff,2} - n_{eff,1})}{\lambda_0} \cdot \frac{\sin(\pi m \gamma)}{m} \quad (2)$$

In order to calculate the LC-RWG grating coupling coefficient correctly one has to be careful about computing n_{eff} and Γ_g when using (1) or about computing n_{eff}, $n_{eff,1}$ and $n_{eff,2}$ when using (2) (either in its accurate left-side form or in its approximate right-side form). Since the transverse optical field distribution does not change from one grating slice to the next, the correct n_{eff} and Γ_g can be calculated, together with the longitudinally-constant transverse optical field distribution, from the longitudinally-averaged transverse refractive index distribution:

$$n_{avg}(x,y) = \sqrt{\gamma n_1(x,y)^2 + (1-\gamma) n_2(x,y)^2} \quad (3)$$

while the effective refractive indices $n_{eff,1}$ and $n_{eff,2}$ can be obtained from the convolution between the longitudinally-constant transverse optical field distribution and the transverse refractive index distributions in the grating slices[13].

Besides the differences in the approximations that can be used for calculating the coupling coefficient, the LC-RWG gratings also interact differently with the optical field. For example, in the buried-gratings the transverse optical field distribution does not change substantially with the grating filling factor (as the longitudinally-averaged transverse refractive index distribution does not change substantially with γ). Consequently, the coupling coefficient variation with the grating filling factor is mainly derived from the variation of the term $\sin(\pi m\gamma)/m$ from (1), whereas the variations of the effective refractive index n_{eff} and of the grating optical confinement factor Γ_g have only a limited influence[14]. However, in the case of LC-RWG gratings, the grating structure parameters (the etching depth, the width of the un-etched central ridge W, the lateral extension of the grating D, the filling factor γ, etc.) have a significant influence on the longitudinally-averaged transverse refractive index distribution and, consequently, on the transverse optical field distribution. An immediate result is that the maximum coupling coefficient is largely dependent on the grating filling factor since a higher filling factor reduces the contrast in the LC-RWG grating region, pulling the optical field into the grating region and increasing the grating confinement factor. Figure 3 illustrates the strong dependence of the coupling coefficient on the filling factor and the fact that the grating trench width is the critical technological parameter, as the coupling coefficient is similar for all grating orders, if the trench width is the same, until the trench width becomes very small. It should be mentioned that the LC-RWG grating structure parameters have also a substantial influence on the transverse mode discrimination, so that a special care must be taken to maintain the single transverse mode operation while attempting coupling coefficient optimization by changing the grating parameters.

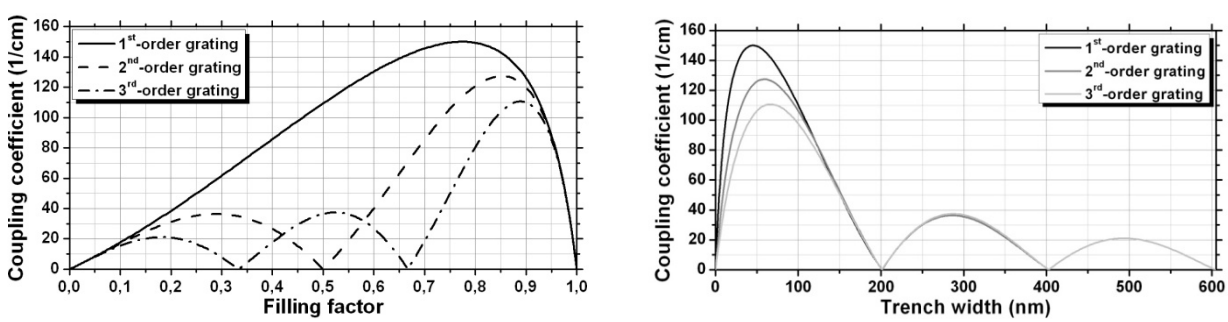

Figure 3. First transverse mode coupling coefficient as a function of the filling factor (left panel) and of the trench width (right panel) for 1st, 2nd or 3rd –order 1.3 μm LC-RWG gratings.

3. MODELING AND SIMULATION OF PHOTON-PHOTON RESONANCE

A modified rate-equation model has been developed to include the PPR by treating the longitudinal quantum well confinement factor as a dynamic variable[15]. The differential rate equations including the extra term resulted from taking the quantum well confinement factor as a dynamic variable are the following:

SPIE USE: ____ DB Check, ____ Prod Check, Notes:

Please verify that (1) all pages are present, (2) all figures are acceptable, (3) all fonts and special characters are correct, and (4) all text and figures fit within the margin lines shown on this review document. Return to your MySPIE ToDo list and approve or disapprove this submission.

$$\frac{d}{dt}\begin{bmatrix} dN \\ dN_p \end{bmatrix} = \begin{bmatrix} -\gamma_{NN} & -\gamma_{NP} \\ \gamma_{PN} & -\gamma_{PP} \end{bmatrix}\begin{bmatrix} dN \\ dN_p \end{bmatrix} + \begin{bmatrix} \frac{\eta_i}{qV} dI \\ (N_p v_g g + R_{sp}^{'}) d\Gamma \end{bmatrix} \tag{4}$$

where γ_{NN}, γ_{NP}, γ_{PN} and γ_{PP} are rate coefficients, as defined in[16]. By following the same analysis of the small-signal response to a sinusoidal current modulation as in [16], the small-signal photon density, including the influence of the extra term results as:

$$N_{p1} = \frac{\eta_i I_1}{qV} \cdot \frac{\gamma_{PN}}{\Delta} + (N_p v_g g + R_{sp}^{'}) \cdot \frac{(\gamma_{NN} + j\omega)}{\Delta} \cdot \frac{d\Gamma}{e^{j\omega t}} \tag{5}$$

where $\Delta = (\gamma_{NN} + j\omega)(\gamma_{PP} + j\omega) + \gamma_{NP}\gamma_{PN}$. The modulation transfer function including the influence of the extra term resulted from the (space and) time variation of the confinement factor, can be written as:

$$H(\omega) = \frac{\eta_i}{qV} \frac{\int_0^T \frac{\gamma_{PN}}{\Delta} dt}{\int_0^T dt} + \frac{1}{I_1 \cdot \int_0^T dt} \cdot \int_0^T \frac{(\gamma_{NN} + j\omega) \cdot (N_p v_g g + R_{sp}^{'})}{\Delta \cdot e^{j\omega t}} \cdot \frac{d\Gamma}{dt} dt \tag{6}$$

where T is the time interval for which the phase difference, $\Delta\varphi$, between the dominant longitudinal modes is maintained. The first term in (6) resembles the traditional modulation transfer function, with γ_{PN} and Δ taken as time-dependent, while the second term is resulted from considering the (space and) time dependence of the confinement factor. This second term of the modulation transfer function introduces the supplementary PPR peak placed at a frequency equal with the frequency difference between the two dominant longitudinal modes. When the two dominant longitudinal modes are consecutive longitudinal modes and their separation is not substantially altered by detuned loading, the PPR frequency occurs at about the round-trip frequency, in agreement with the experimental results reported in [17-20].

Simulated modulation responses, including the contribution of the supplementary transfer function term, for a 1000 µm long laser structure biased at 100 mA (with typical material parameters) and emitting at 1.3 µm on two dominant longitudinal modes with 40 GHz frequency separation, are illustrated in Figure 4. The modulation responses have been calculated for SMSR values between the two dominant longitudinal modes ranging from 10 to 60 dB.

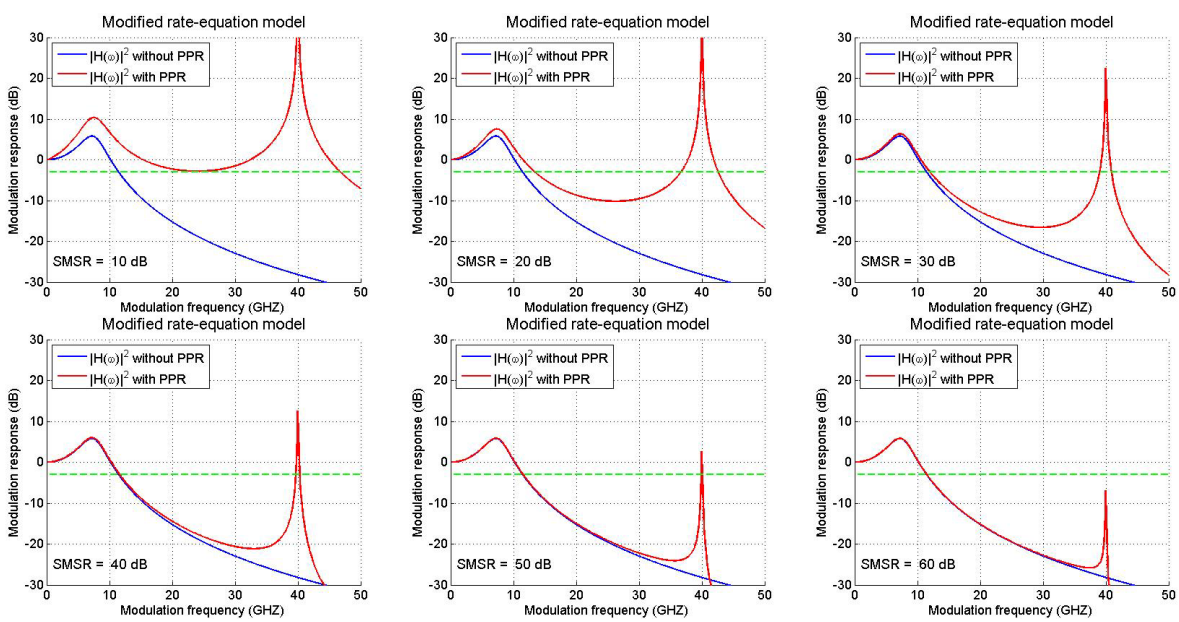

Figure 4. Simulated small-signal modulation responses for a 1 mm long laser structure emitting at 1.3 µm on two dominant longitudinal modes with 40 GHz frequency separation, for different SMSRs between these modes.

SPIE USE: ____ DB Check, ____ Prod Check, Notes:

Please verify that (1) all pages are present, (2) all figures are acceptable, (3) all fonts and special characters are correct, and (4) all text and figures fit within the margin lines shown on this review document. Return to your MySPIE ToDo list and approve or disapprove this submission.

More advanced simulations, based on the Finite Difference Time Domain (FDTD) method[21-23] have been carried out in order to identify the conditions under which the PPR occurs and leads to an extended modulation bandwidth. The simulations have indicated that the end-mirror reflectivities and their phase relationship with the grating reflections, the bias level, the gain compression factor and the linewidth enhancement factor play a significant role in having a modulation response extended by the presence of a substantial PPR peak and exhibiting relative flatness between the CPR and PPR peaks.

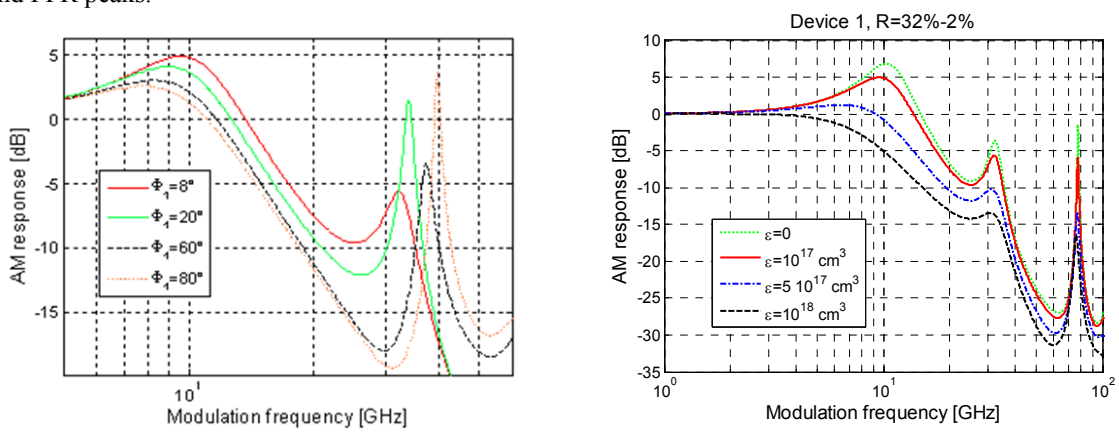

Figure 5. Amplitude modulation response for end-mirror phase Φ_1=8°,20°,60° and 80° (left panel) and for different gain compression factor values (right panel)

The left panel of Figure 5 shows the variation of the modulation bandwidth when the phase of the as-cleaved end-facet mirror is changed (with the other end-facet mirror being anti-reflection coated) while the right panel of Figure 5 shows the modulation bandwidth for different values of the gain compression factor (ε), when the cleaved mirror phase is Φ_1=8° and the linewidth enhancement factor is equal to 2. The simulation results confirmed that a high gain compression factor strongly reduces both the carrier-photon and the photon-photon resonance peaks and illustrate the difficulty in achieving a relatively flat modulation response between the CPR and PPR. Figure 6 shows the modulation response calculated assuming a relatively small gain compression factor of 10^{17} cm^3 and a linewidth enhancement factor varying from 1 to 3 for two levels of bias (lower in the left panel and higher in the right panel). It can be observed that, when the bias is increased, the CPR frequency increases and the dip between the CPR and the PPR is reduced, leading, in the analyzed case, to a -3dB modulation bandwidth of around 37 GHz for a linewidth enhancement factor of 2.

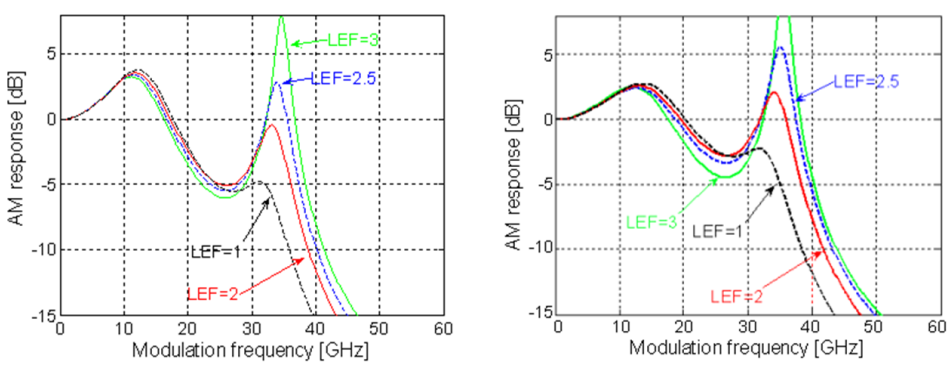

Figure 6. Amplitude modulation response for different values of the linewidth enhancement factor, when Φ_1=8° and I=8*I_{th} (left panel) and I=12*I_{th} (right panel).

4. INCREASING THE LC-RWG GRATING COUPLING COEFFICIENT

An important requirement for achieving a stable PPR was found to be a high grating coupling coefficient. Several methods have been investigated for increasing the LC-RWG grating coupling coefficient: adjusting the epilayer structure, reducing the width of the un-etched central section of the ridge W, increasing the lateral extension of the grating D, using lower order gratings and increasing the grating filling factor. Reducing the p-side cladding thickness in order to enable achieving a higher coupling coefficient with less deep etching was not applied since the p-side cladding

SPIE USE: ____ DB Check, ____ Prod Check, Notes:

Please verify that (1) all pages are present, (2) all figures are acceptable, (3) all fonts and special characters are correct, and (4) all text and figures fit within the margin lines shown on this review document. Return to your MySPIE ToDo list and approve or disapprove this submission.

was (in most cases) already close to the thickness that would induce optical field coupling into the contact. Altering the epilayer structure for extending the optical field penetration into the p-side cladding in order to increase the grating confinement factor Γ_g was also ruled out because, besides potential optical field coupling with the contact, it leads to the decrease in the quantum well confinement factor, which affects adversely the laser characteristics. Also reducing too much the width of the un-etched central section of the ridge, W, affects adversely the electrical characteristics of the laser (increased resistance and operating voltage) and increases the difficulty of aligning the contact opening. Regarding the lateral extension of the gratings, D, the simulations have pointed out that the coupling coefficient increase saturates with increasing D but have also indicated that the experimentally-determined LC-RWG grating coupling coefficients for the first device batches were significantly smaller than predicted.

The analysis of the discrepancies between the simulated and experimentally-determined coupling coefficients showed that technologically-induced imperfect grating profiles play a significant role in reducing the grating coupling coefficient. The left panel of Figure 7 shows a scanning electron microscopy (SEM) image of an imperfect LC-RWG grating profile caused by aspect-ratio-dependent-etching (ARDE). The imperfect grating profiles exhibit un-etched pockets at the bottom of the grating trenches, towards the ridge, exactly in the areas where the optical field should couple with the gratings. The middle panel of Figure 7 illustrates improved etching profiles obtained by adjusting the process parameters and by using a more uniform distribution of the areas to be etched across the processed area. Since a large lateral extension, D, of the LC-RWG gratings could lead to increased lateral leakage of the pump current, an improved structure, with recessed upper gratings (for limiting the lateral current flow into the gratings) and a large lateral extension of the grating at the bottom to increase κ (shown in the right panel of Figure 7), was also developed.

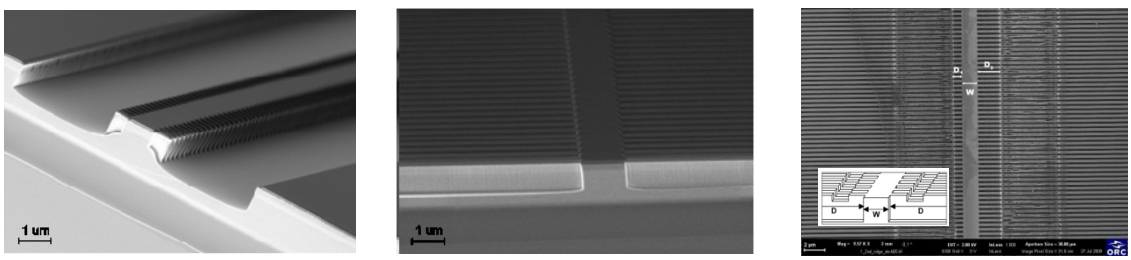

Figure 7. SEM images of the LC-RWG grating profile with un-etched pockets caused by ARDE (left panel), of the improved LC-RWG grating profile obtained by reducing the ARDE effect (middle panel) and of the LC-RWG grating structure with a top recess for limiting the lateral current leakage into the gratings (right panel)

Process trials have been carried out to test the fabrication of LC-RWG gratings with lower order and/or higher filling factors, mainly for achieving a higher κ. Figure 8 shows SEM pictures of LC-RWG gratings etched 1.1-1.2 µm deep in GaAs/AlGaAs with a Λ=180nm period and variable filling factor. While the gratings with low filling factor $\gamma=\Lambda_1/\Lambda$=40/180 (in the leftmost panel) were deformed and broke during the cleaving, the gratings with higher filling factor γ=60/180 and γ=80/180 (in the second and third panels from left) were stable, pointing out that the difficulty is less in obtaining narrow trenches and more in obtaining narrow and stable grating 'wings'.

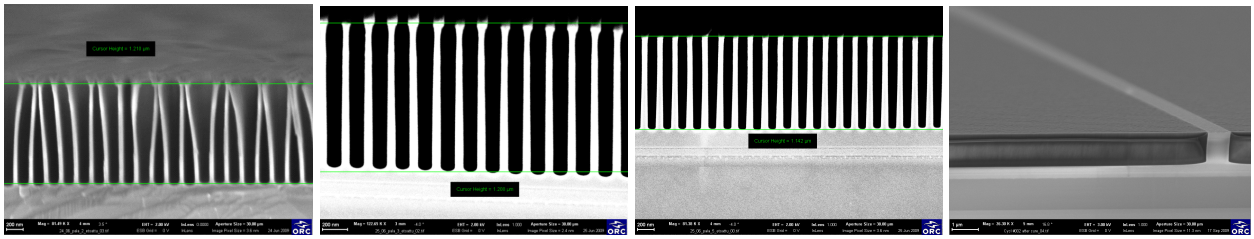

Figure 8. Cross section SEM views of LC-RWG gratings with Λ=180 nm period and trench widths Λ_2 of 140, 120 and 100 nm (first, second and third panel from left, respectively) together with a SEM view of LC-RWG gratings after BCB polymer filling (right panel)

To ensure the gratings' mechanical stability, plasma enhanced chemical vapour deposition of SiO_2 was used in the first trials but, since it was found that it leads to incomplete filling of high aspect ratio grating trenches, it was replaced by benzocyclobutene (BCB) polymer filling. The BCB filling tests, illustrated in the right panel of Figure 8, indicate that the BCB filling, beside providing mechanical stability and passivating the device surface, also decreases the scattering losses and reduces the thermal resistance of the devices.

SPIE USE: ____ DB Check, ____ Prod Check, Notes:

Please verify that (1) all pages are present, (2) all figures are acceptable, (3) all fonts and special characters are correct, and (4) all text and figures fit within the margin lines shown on this review document. Return to your MySPIE ToDo list and approve or disapprove this submission.

5. DFB AND DBR LASER CHARACTERISTICS

Laterally-coupled distributed feedback (LC-DFB) and distributed Bragg reflector (LC-DRB) lasers with LC-RWG gratings have been fabricated from legacy epiwafers (with pre-existing epilayer structures, not specially designed to be used with LC-RWG gratings) at 1.3 and 1.55 µm. Various structures have been fabricated and characterized, from simple single-longitudinal-section DFB laser structures with uniform or structured/non-uniform gratings to DBR laser structures with multiple longitudinal sections (e.g. gain, grating and phase sections). Figure 9 shows the sketches of the main laser structures that were tested and fabricated besides the straightforward LC-DFB structures: two section (grating and gain) LC-DBR laser structure (left panel) and three-section (phase, grating and gain) LC-DBR laser structure (right panel) together with a SEM image of the gain-grating junction area of a fabricated LC-DBR laser (middle panel).

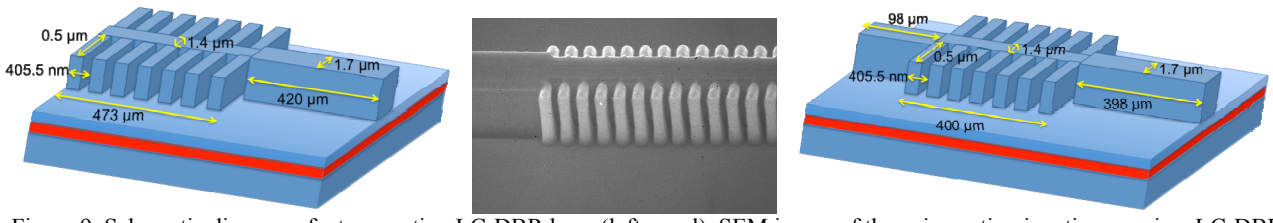

Figure 9. Schematic diagram of a two-section LC-DBR laser (left panel), SEM image of the gain-grating junction area in a LC-DBR laser (middle panel) and schematic diagram of a three-section LC-DBR laser (right panel)

Although the use of several separate contacts enables a supplementary flexibility in achieving the operating conditions needed for obtaining a PPR-extended modulation bandwidth, we have focused on trying to achieve the PPR-extended modulation bandwidth with single-contact (single drive current) devices, which are beneficial from the module fabrication point of view, even if the devices have a complex longitudinal structure. In this respect we have first fabricated and characterized LC-DFB lasers, targeting a high CPR frequency, and followed with multiple-section and multiple-contact devices, targeting the identification of operating conditions enabling PPR, with the final goal to identify the structures and operating conditions enabling PPR-extended modulation bandwidth with a single drive current.

1.3 µm LC-DFB lasers have been processed from AlGaInAs/InP legacy epiwafers by a combination of E-beam lithography and electron cyclotron resonance (ECR) dry etching. The lasers had third-order LC-RWG gratings, etched down to 150 nm from the separate confinement heterostructure (SCH) layer, with a target filling factor of 0.5, a central un-etched ridge width W=2 µm and a lateral extension of the gratings D=5 µm. No facet coating was applied to the devices and all the reported 1.3 µm measurements were performed on 300 µm long DFB lasers. The left panel of Figure 10 shows the output power and current-voltage characteristic of such a 1.3 µm LC-DFB laser. The threshold current is 30 mA and an output power of over 10 mW is reached at a current of 150 mA. The output power is limited by thermal roll-over due to the large series resistance of the device (17 Ohm), which was caused by the initial fabrication process that incorporated the metal etch mask into the p-side contact. The fabrication process has been corrected to resolve this issue but all the devices discussed in this paper have been fabricated using un-optimized processes.

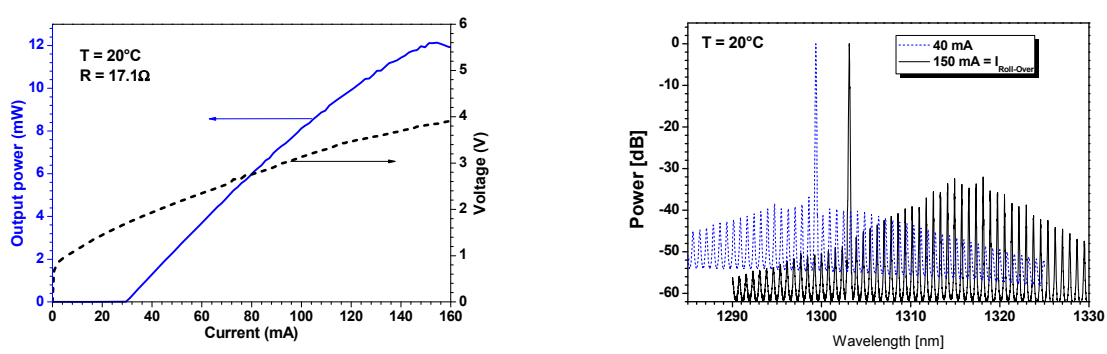

Figure 10: Output power and current-voltage characteristic at room temperature for a 300 µm long 1.3 µm LC-DFB laser (left panel) and emission spectrum of the laser for 40 and 150 mA bias currents (right panel)

The maximum temperature at which these 1.3 µm lasers work as single-mode DFB lasers is 55°C. There are several reasons for the limited temperature range of single mode operation. First, the high resistance of the devices leads to a

SPIE USE: ____ DB Check, ____ Prod Check, Notes:

Please verify that (1) all pages are present, (2) all figures are acceptable, (3) all fonts and special characters are correct, and (4) all text and figures fit within the margin lines shown on this review document. Return to your MySPIE ToDo list and approve or disapprove this submission.

considerable amount of excess heat, substantially increasing the internal temperature. Second, as the LC-RWG grating geometry affects both the coupling coefficient and the transverse modal behavior, a large lateral extension of the grating favors higher order transverse modes. Third, the LC-RWG grating coupling coefficient in these devices is only around 10 cm^{-1}. The low coupling coefficient value, largely determined by an imperfect etching profile, is sufficient to induce single-mode operation with a high side-mode-suppression-ratio (SMSR) when the Bragg resonance wavelength and the peak of the gain are close, but does not enable single-mode operation for larger spacing between the Bragg resonance wavelength and the gain peak. The right panel of Figure 10 shows the laser spectrum for two different bias currents: one just above threshold (40 mA) and the other (150 mA) where the laser starts to roll over. The shift of the DFB-mode is 3.77 nm and the gain peak shift is about 14-15 nm. More detailed plots of the emission spectra variation with the bias current and with the ambient temperature are given in Figure 11. The shift of the emission wavelength increases with increasing bias current due to the quadratic dependence of the ohmic losses on the drive current. On the other hand, the shift of the emission wavelength with temperature was constant at 0.09nm/K.

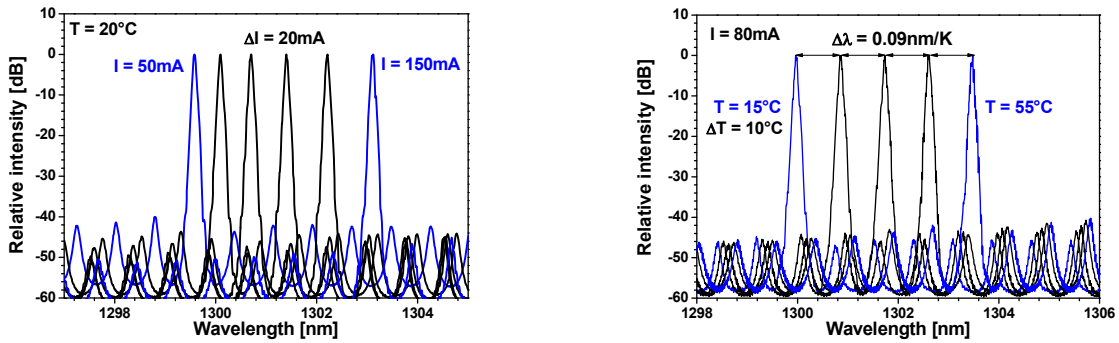

Figure 11. Emission spectra at 20°C for bias currents between 50 and 150 mA (left panel) and emission spectra at 80 mA bias for temperatures between 15 and 55°C (right panel)

Measurements of the modulation bandwidth and of the relative intensity noise have also been performed on these InP-based 1.3 µm LC-DFB lasers. The left panel of Figure 12 shows the modulation response of the 1.3 µm LC-DFB laser at room temperature under different bias currents. The maximum modulation bandwidth for single mode operation is 16 GHz, obtained at a current of 150 mA. If the current is increased to 160 mA, the modulation bandwidth is increased further to 16.2 GHz, but the laser is no longer single mode. For even higher currents, beyond the thermal roll-over, the modulation bandwidth decreases, as expected, due to self-heating effects. The modulation bandwidth variation with bias was used to extract the resonance frequency and the damping. The squared CPR frequency dependence on the output power of the laser can be fitted by a linear variation with a slope of 12.3 GHz^2/mW.

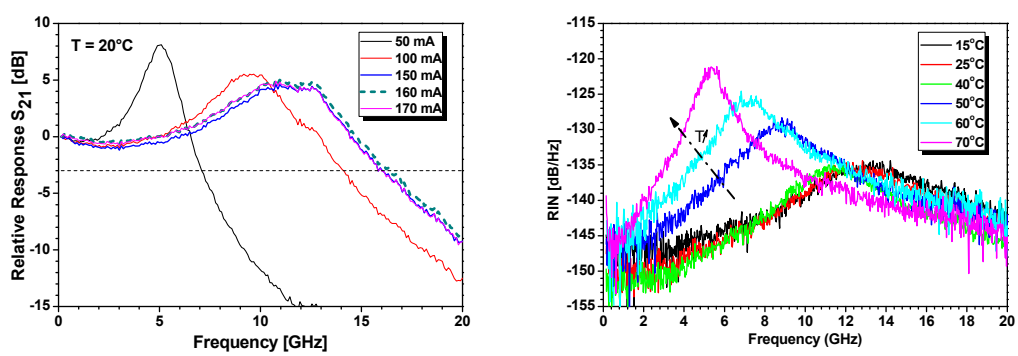

Figure 12. Small signal response at room temperature for different bias currents (left panel) and relative intensity noise at temperatures between 15 and 70°C (right panel) for the 300 µm long InP-based 1.3 µm LC-DFB lasers

The right panel of Figure 12 shows the relative intensity noise (RIN) variation with temperature for these 1.3 µm LC-DFB lasers. As expected, the largest CPR frequency of 13 GHz is obtained for the lowest temperature (15°C) and it decreases as the temperature is increased. For temperatures above 60°C, an increase of the relative intensity noise for frequencies below 200 MHz is observed, which can be attributed to the fact that the lasers are multi-mode above 55°C.

7953 - 12 V. 2 (p.8 of 12) / Color: No / Format: A4 / Date: 2011-02-03 04:15:41 PM

SPIE USE: ____ DB Check, ____ Prod Check, Notes:

Please verify that (1) all pages are present, (2) all figures are acceptable, (3) all fonts and special characters are correct, and (4) all text and figures fit within the margin lines shown on this review document. Return to your MySPIE ToDo list and approve or disapprove this submission.

1.55 µm LC-DFB lasers have also been processed from AlGaInAs/InP legacy epiwafers using a similar LC-RWG grating geometry (except for the grating period) and a similar fabrication procedure as for the 1.3 µm LC-DFB lasers. The left panel of Figure 13 shows a SEM view of the 1.55 µm LC-DFB laser facet illustrating the LC-RWG grating profile. The middle panel of Figure 13 gives the ILV characteristics of a 800 µm long 1.55 µm LC-DFB laser with as-cleaved facets (the output power is given per one facet), whereas the right panel of Figure 13 shows the emission spectra at a bias just above threshold (40 mA) and at a bias just below the thermal roll-over (200 mA). The 1.55 µm LC-DFB lasers have a smaller series resistance, due to improved processing, have a high SMSR and exhibit better single-mode operation stability. These lasers are single mode over the whole operation range, although the LC-RWG grating coupling coefficient is still small, because of their higher κL product.

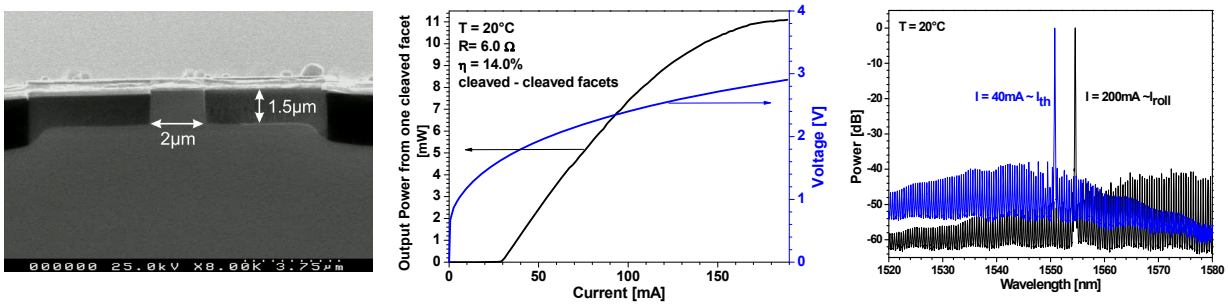

Figure 13. SEM image of 1.55 µm LC-DFB laser facet (left panel), ILV characteristics of 800 µm long LC-DFB laser with as-cleaved facets (middle panel) and emission spectra just above the threshold and just below the roll-over bias (right panel)

300 µm long 1.55 µm Fabry-Perot lasers, specially designed and fabricated for high-speed operation (at III-V Lab) have achieved up to 19 GHz small-signal modulation bandwidth, as illustrated in Figure 14.

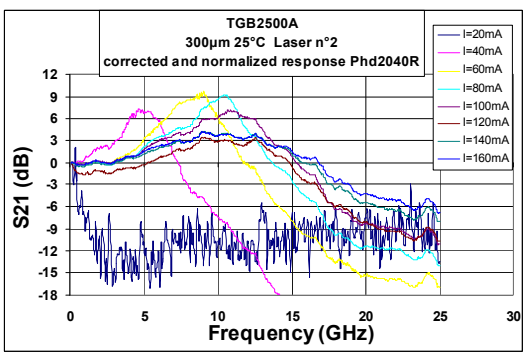

Figure 14. Modulation response of a 300 µm long 1.55 µm high-speed Fabry-Perot laser at different bias currents

Multi-section lasers in their turn have also exhibited stable single-mode operation with a good SMSR both at 1.3 and at 1.55 µm, as illustrated in Figure 15.

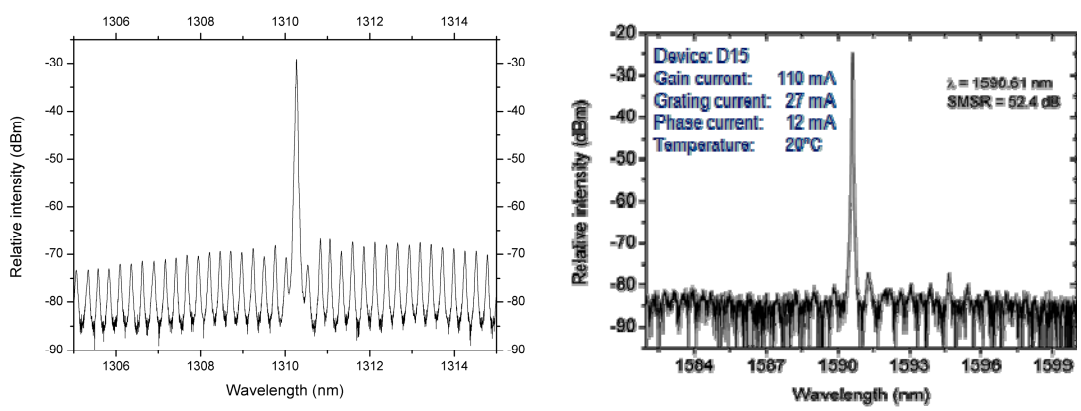

Figure 15. Emission spectra from two section (left panel) and three-section (right panel) LC-DBR lasers exhibiting high SMSRs

SPIE USE: ____ DB Check, ____ Prod Check, Notes:

Please verify that (1) all pages are present, (2) all figures are acceptable, (3) all fonts and special characters are correct, and (4) all text and figures fit within the margin lines shown on this review document. Return to your MySPIE ToDo list and approve or disapprove this submission.

Beyond the good performances of the fabricated single and multi-section lasers, the most important achievement was the realization of single contact lasers exhibiting extended modulation bandwidth based on PPR. Figure 16 shows the modulation response of a 1.6 mm long longitudinally-structured single-contact LC-DFB laser at different bias currents.

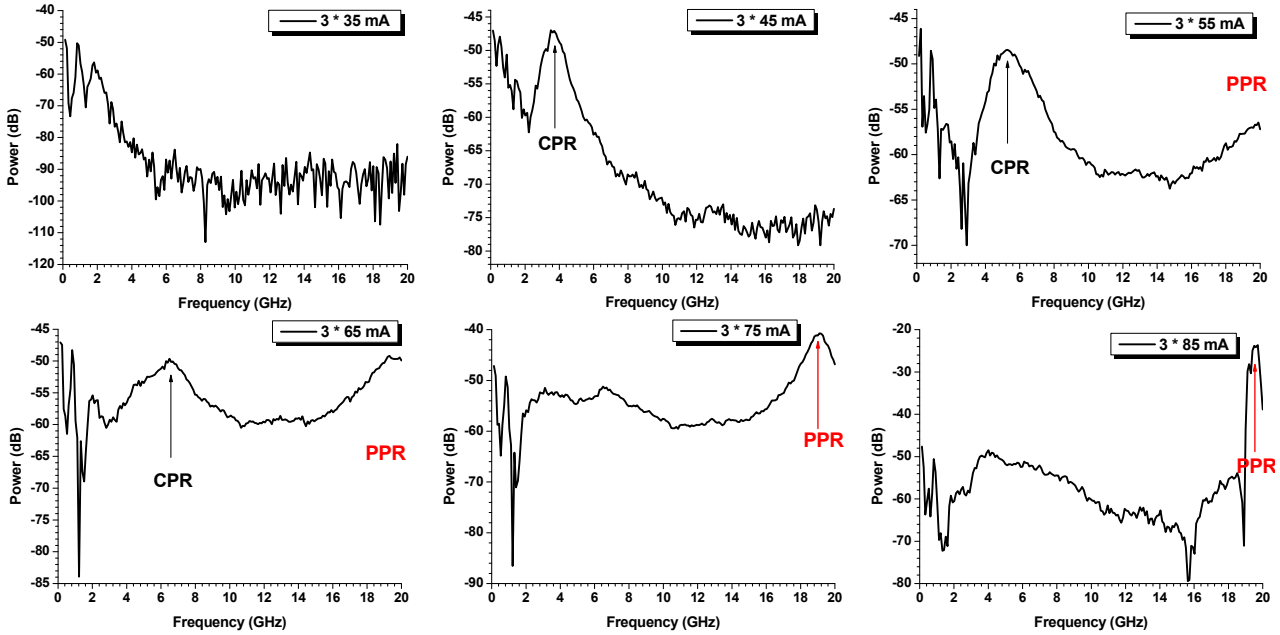

Figure 16. Modulation response of a single-contact 1.6 mm long 1.55 µm LC-DFB laser at different bias currents

The panels of Figure 16 show that the PPR peak is enhanced at higher bias and that at certain bias currents the modulation response is relatively flat between the CPR and PPR. It should be mentioned that the PPR frequency is relatively stable under single-contact operation, being imposed by the longitudinal geometry of the devices. Figure 17 shows the RIN spectra obtained from the same single-contact device and at the same bias currents with those used for the modulation response measurements given in Figure 16. It can be observed that above a certain bias level there is a clear and sharp PPR peak in the RIN spectra at a frequency that does not change substantially with the bias, being imposed by the longitudinal device geometry. The RIN peak around 23.5 GHz is a measurement system artifact.

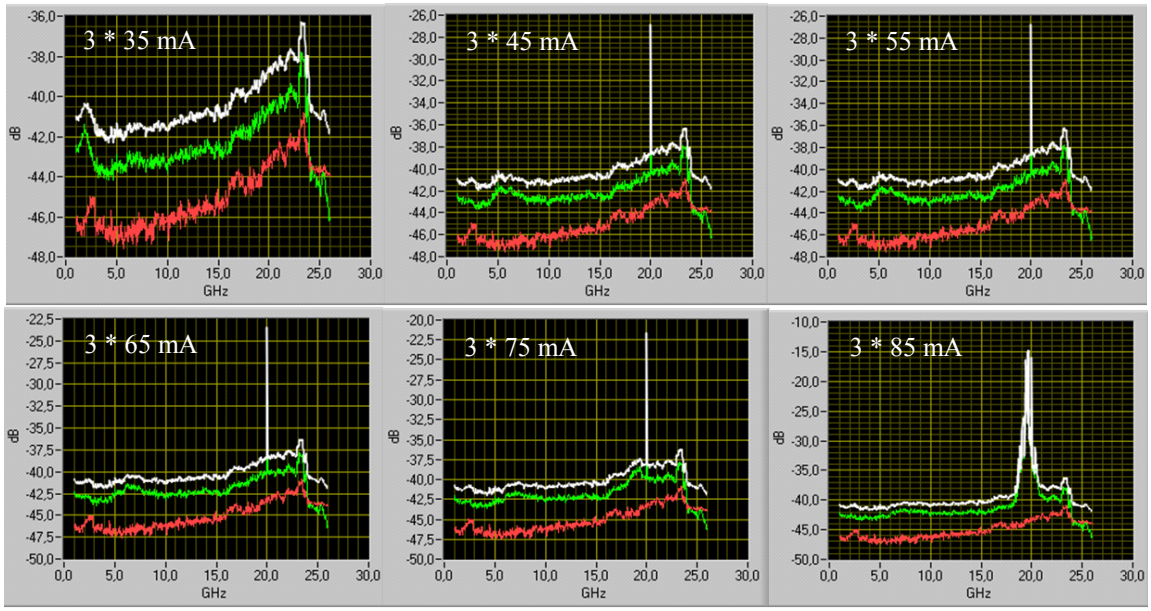

Figure 17. RIN spectra at different bias currents for a single-contact 1.6 mm long 1.55 µm LC-DFB laser

7953 - 12 V. 2 (p.10 of 12) / Color: No / Format: A4 / Date: 2011-02-03 04:15:41 PM

SPIE USE: ____ DB Check, ____ Prod Check, Notes:

Please verify that (1) all pages are present, (2) all figures are acceptable, (3) all fonts and special characters are correct, and (4) all text and figures fit within the margin lines shown on this review document. Return to your MySPIE ToDo list and approve or disapprove this submission.

Although the main goal was to obtain the PPR-extended modulation bandwidth under single contact/current operation, we have also studied the possibility to adjust the modulation bandwidth by using multiple drive currents. The left panel of Figure 18 shows the tuning of the PPR frequency by adjusting one of the drive currents while the middle panel of Figure 18 shows the adjustments in the modulation response flatness obtained by changing another drive current of the 1.6 mm long LC-DFB laser operated as a multi-contact/current device. The right panel of Figure 18 points out to the possibility of increasing the PPR frequency of this device beyond 20 GHz.

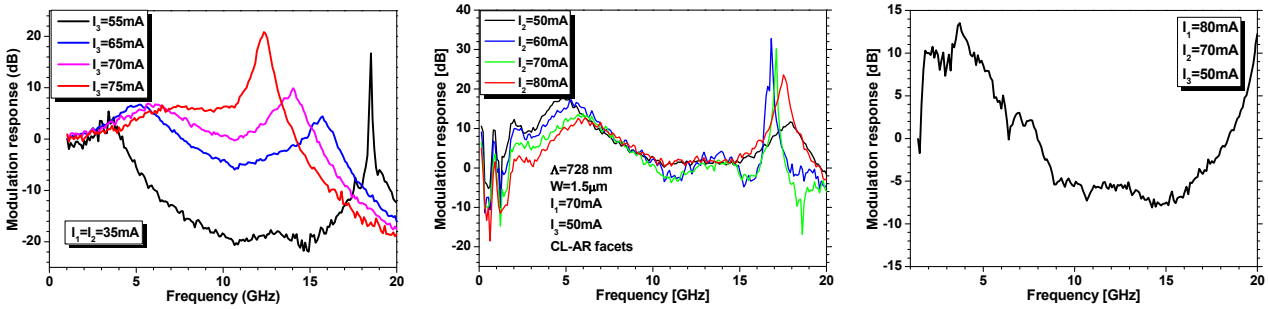

Figure 18. PPR tuning under multiple-contact operation (left panel), adjusting the modulation response flatness between the CPR and PPR (middle panel) and PPR beyond 20 GHz (right panel) for the 1.6 mm long 1.55 μm LC-DFB laser

6. CONCLUSIONS

Laterally-corrugated ridge waveguide (LC-RWG) surface gratings have been studied and developed in order to simplify the fabrication of conventional DFB and DBR lasers with buried gratings. The particularities of LC-RWG gratings, in terms of their interaction with the optical field, in terms of calculating their coupling coefficient and its dependencies on grating geometry and in terms of technological fabrication possibilities and limitations, have been investigated. It was found that the grating trench width is largely governing the LC-RWG grating coupling coefficient and that, from the technological point of view, the etching aspect ratio is the most important restriction while a good etching profile is the most important requirement. The possibilities and limitations in achieving high coupling coefficients with LC-RWG gratings have been analyzed. LC-DFB and LC-DBR lasers employing LC-RWG gratings have been designed and fabricated at 1.3 and 1.55 μm, proving that the use of LC-RWG gratings is a valid alternative with multiple potential advantages over the conventional buried grating.

The exploitation of the photon-photon resonance (PPR) for increasing the direct modulation bandwidth beyond the limitations set by the carrier-photon resonance has been studied and devices with PPR-extended modulation bandwidth have been designed, simulated and fabricated. It was demonstrated that single-contact / single-drive-current lasers employing LC-RWG gratings can achieve stable PPR, leading to a substantial modulation bandwidth increase. The first experimental results (showing >20 GHz PPR-enhanced direct-modulation bandwidth from a 1.6 mm long laser employing LC-RWG gratings) and the simulation studies (indicating that >40 GHz direct modulation bandwidth can be obtained from shorter devices with similar structure) point out to the possibility of fabricating low-cost directly-modulated lasers with modulation bandwidths in excess of 40 GHz.

ACKNOWLEDGEMENTS

The results reported in the paper have been obtained within the European Commission EU FP7 ICT-224366 project "Development of low-cost technologies for the fabrication of high-performance telecommunication lasers (DeLight)" (www.delightproject.eu).

7953 - 12 V. 2 (p.11 of 12) / Color: No / Format: A4 / Date: 2011-02-03 04:15:41 PM

SPIE USE: ____ DB Check, ____ Prod Check, Notes:

Please verify that (1) all pages are present, (2) all figures are acceptable, (3) all fonts and special characters are correct, and (4) all text and figures fit within the margin lines shown on this review document. Return to your MySPIE ToDo list and approve or disapprove this submission.

REFERENCES

[1] Arakawa, Y., Vahala, K., and Yariv, A., "Quantum noise and dynamics in quantum well and quantum wire lasers," Appl. Phys. Lett. 45(9), 950–952 (1984).

[2] Suemune, I., Coldren, L. A., Yamanishi, M., and Kan, Y., "Extremely wide modulation bandwidth in a low threshold current strained quantum well laser," Appl. Phys. Lett. 53(15), 1378–1380 (1988).

[3] Nagarajian, R., Ishikawa, M., Fukushima, T., Geels, R. S., and Bowers, J. E., "High speed quantum-well lasers and carrier transport effects," IEEE J. Quantum Electron. 28(10), 1990–2008 (1992).

[4] Deppe, D. G., Huang, H., and Shchekin, O. B., "Modulation characteristics of quantum-dot lasers: The influence of P-type doping and the electronic density of states on obtaining high speed," IEEE J. Quantum Electron. 38(12), 1587–1593 (2002).

[5] Kim, S. M., Wang, Y., Keever, M., and Harris, J. S., "High-frequency modulation characteristics of 1.3-μm InGaAs quantum dot lasers," IEEE Photon. Technol. Lett. 16(2), 377–379 (2004).

[6] Fathpour, S., Mi, Z., and Bhattacharya, P. "High-speed quantum dot lasers," J. Phys. D 38(13), 2103–2111 (2005).

[7] Kuntz, M., Fiol, G., Lämmlin, M., Schubert, C., Kovsh, A. R., Jacob, A., Umbach, A., and Bimberg, D., "10 Gbit/s data modulation using 1.3 μm InGaAs quantum dot lasers," Electron. Lett. 41(5), 244–245 (2005).

[8] Kaminow, I., Li, T., and Willner, A., eds., [Optical Fiber Telecommunications V A: Components and Subsystems], Elsevier, Ch. 3 and 6 (2008).

[9] Lang, R., and Kobayashi, K., "Suppression of the relaxation oscillation in the modulated output of semiconductor lasers," IEEE J. Quantum Electron. 12(3), 194–199 (1976).

[10] Wang, J., Haldar, M. K., Li, L., and Mendis, F. V. C., "Enhancement of modulation bandwidth of laser diodes by injection locking," IEEE Photon. Technol. Lett. 8(1), 34–36 (1996).

[11] Deppe, D. G., and Huang, H., "Quantum-dot vertical-cavity surface-emitting laser based on the Purcell effect," Appl. Phys. Lett. 75(22), 3455–3457 (1999).

[12] Altug, H., Englund, D., and Vuckovic, J., "Ultrafast photonic crystal nanocavity laser," Nat. Phys. 2(7), 484–488 (2006).

[13] Laakso, A., Dumitrescu, M., Viheriälä, J., Karinen., J., Suominen, M., and Pessa, M., "Optical modeling of laterally-corrugated ridge-waveguide gratings," Opt. Quantum Electron. 40(11-12), 907-920 (2008).

[14] Dumitrescu, M., Telkkälä, J., Karinen, J., Viheriälä, J., Laakso, A., Haring, K., Viljanen, M.-R., Paajaste, J., Koskinen, R., Suomalainen, S., Lyytikäinen, J., Leinonen, T., Pessa, M., "Narrow-linewidth distributed feedback lasers with laterally-coupled ridge-waveguide surface gratings fabricated using nanoimprint lithography," Proc. SPIE 7953-10, (2011).

[15] Laakso, A., and Dumitrescu, M., "Modified rate equation model including the photon-photon resonance", IEEE Proc. 10th Int. Conf. on Numerical Simulation of Optoelectronic Devices (NUSOD), 117-118 (2010).

[16] Coldren, L. A., and Corzine, S. W., [Diode Lasers and Photonic Integrated Circuits], Wiley, New York (1995).

[17] Bach, L., Kaiser, W., Reithmaier, J. P., Forchel, A., Gioannini, M., Feies, V., and Montrosset, I., "22-GHz Modulation Bandwidth of Long Cavity DBR Laser by Using a Weakly Laterally Coupled Grating Fabricated by Focused Ion Beam Lithography," IEEE Photon. Technol. Lett., 16(1), 18-20 (2004).

[18] Kaiser, W., Bach, L., Reithmaier, J. P., and Forchel, A., "High-Speed Coupled-Cavity Injection Grating Lasers With Tailored Modulation Transfer Functions," IEEE Photon. Technol. Lett. 16(9), 1997-1999 (2004)

[19] Gerschütz, F., Fischer, M., Koeth, J., Krestnikov, I., Kovsh, A., Schilling, C., Kaiser, W., Höfling, S., and Forchel, A., "1.3 μm Quantum Dot Laser in coupled-cavity-injection-grating design with bandwidth of 20 GHz under direct modulation," Opt. Express 16(8), 5596-5601 (2008).

[20] Radziunas, M., Glitzky, A., Bandelow, U., Wolfrum, M., Troppenz, U., Kreissl, J., and Rehbein, W., "Improving the Modulation Bandwidth in Semiconductor Lasers by Passive Feedback," IEEE J. Sel. Top. Quantum Electron. 13(1), 136-142 (2007).

[21] Vizzino, A., Gioannini, M., and Montrosset, I., "Dynamic simulation of clock recovery with self-pulsating three-section distributed-feedback lasers", IEEE J. Quantum Electron. 38(12), 1580-1586 (2002).

[22] Bardella, P., Montrosset, I., "Analysis of self-pulsating three-section DBR lasers", IEEE J. Sel. Top. Quant. Electron. 11(2), 361-366 (2005).

[23] Vallone, M., Bardella, P., Montrosset, I., "Photon-photon resonance enhanced modulation bandwidth in CCIG lasers", Proc. 15th European Conf. on Integrated Optics – ECIO, ThP16 (2010).

7953 - 12 V. 2 (p.12 of 12) / Color: No / Format: A4 / Date: 2011-02-03 04:15:41 PM

SPIE USE: ____ DB Check, ____ Prod Check, Notes: